Direct 12-Electron Oxidation of Ethanol on a Ternary Au(core)-PtIr(shell) Electrocatalyst

Zhixiu Liang[†], Liang Song[†], Shiqing Deng[‡], Yimei Zhu[‡], Eli Stavitski[§], Radoslav R. Adzic,[†] Jingyi Chen,[⊥]* and Jia X. Wang†*

[†]Chemistry Division, Brookhaven National Laboratory, Upton, New York 11973, United States
[‡]Condensed Matter Physics and Materials Science Department, Brookhaven National Laboratory, Upton, New York 11973, United States
[§]National Synchrotron Light Source II, Brookhaven National Laboratory, Upton, New York 11973, United States
[⊥]Department of Chemistry and Biochemistry, University of Arkansas, Fayetteville, AR 72701, United States

Abstract:

Understanding the roles of metals and atomic structures in activating various elementary steps of electrocatalytic reactions can help rational design of binary or ternary catalysts for promoting activity toward desirable products via favorable pathways. Here we report on a newly developed ternary Au@PtIr core-shell catalyst for ethanol oxidation reaction (EOR) in alkaline solutions, which exhibits an activity enhancement of three orders of magnitude compared to AuPtIr alloy catalysts. Analysis of *in situ* infrared reflection absorption spectra for Au@PtIr and its bimetallic subsets, Au@Pt, and PtIr alloy, found that monoatomic steps and Au-induced tensile strain on PtIr facilitate C-C bond splitting via ethanol dissociative adsorption and Ir promotes dehydrogenation at low potentials. As evidenced by the CO band being observed only for the PtIr alloy that is rather inactive for ethanol dissociative adsorption, we propose that splitting the C-C bond at the earliest stage of EOR activates a direct 12-electron full oxidation pathway because hydrogen-rich fragments can be fully oxidized without CO as a poisoning intermediate. The resulting synergy of complementary effects of Au core and surface Ir leads to an outstanding performance of Au@PtIr for EOR as characterized by a low onset potential of 0.3 V and 8.3 A $mg^{-1}_{all\text{-}metals}$ peak current with 57% currents generated via full ethanol oxidation.

INTRODUCTION

Direct ethanol fuel cells using proton exchange membrane or anion exchange membrane are attractive power sources for portable devices due to the high energy density of the fuel and system.[1–3] Each ethanol molecule can release 12 electrons (12e) via a complete electrooxidation: $CH_3CH_2OH + 3H_2O = 2CO_2 + 12H^+ + 12e^-$, which involves cleavage of the C-C bond and multiple dehydrogenation and oxidation steps. However, incomplete ethanol oxidation reaction (EOR), often occurs with 4e transfer producing acetic acid (CH_3COOH) in acid or acetate (CH_3COO^-) in base. The two pathways are termed as C1-12e and C2-4e pathways, respectively, referring to the number of carbon atoms in the products and the number of electrons transferred per ethanol molecule.[4] Various binary and ternary metal/oxide catalysts were studied for improving the EOR efficiency via higher C1-12e selectivity, lower onset potential, and higher peak current than on Pt or Pd.[2,4] In acidic media, a ternary $PtRhSnO_2$ catalyst was the first one showing a 12e EOR to CO_2 at low potentials.[5] The optimal composition, $PtRh_{1/3}SnO_2$, yields a peak current of 1.5 A mg^{-1} platinum group metal (PGM) and a current of 0.14 A mg^{-1} PGM after 1 h at 0.45 V.[6] In alkaline media, Pd-based catalysts[7–14] outperform Pt-based catalysts[15–17] with the peak current reaching 40 A mg^{-1} PGM on Au/Ag/Pd alloy aerogels.[8] The progress for higher PGM activity at peak current is very encouraging, but more attention is needed to lower the onset potential and improve the C1-12e selectivity. Here, we describe a ternary Au(core)-PtIr(shell) catalyst supported on carbon, Au@PtIr/C, which exhibits not only a high peak current of 58 A mg^{-1} PGM but also a low onset potential and a high selectivity toward C1-12e EOR. Comparison with baseline and top performing catalysts is made to facilitate understanding of material trend for EOR in base with that for EOR in acid as a reference.

From a fundamental research point of view, EOR attracts considerable attention as a multi-step reaction with the reaction selectivity and kinetics highly sensitive to atomic structure of metal and metal oxide surfaces.[18,19] For rational design, we need to better understand the effects of various metals and structures in promoting C1-12e selectivity, lower the onset potential, and enhance the peak current. Infrared spectroscopy,[5,20–22] differential electrochemical mass spectroscopy,[23] and ^{13}C NMR spectroscopy[24] have been used to identify and quantify EOR intermediates and products. In this study, we determined, using *in situ* infrared reflection absorption spectroscopy (IRRAS), the key reaction intermediates for EOR in alkaline solution on Au@PtIr/C and its subset catalysts, Au@Pt/C and PtIr/C (Pt:Ir 1:1 alloy particles). Carbonate, a C1-12e product in base, was observed for EOR on Au@PtIr/C and Au@Pt/C, but not on PtIr/C.

Instead, adsorbed CO was found on PtIr/C. The results reveal the key roles of Au-induced lattice expansion and surface steps of nano-islands in enabling a direct C1-12e pathway. Cleavage of the C-C bond at the very beginning of EOR prevents the formation of too strongly adsorbed CO, resulting in preferable C1-12e selectivity and exceptional EOR activity. Ir is identified as a dehydrogenation promoter that mainly contributes in lowering the onset potential.

RESULTS AND DISCUSSION

Synthesis and structural characterization. We synthesized PtIr on carbon supported Au (Au/C) nanoparticles by simultaneously reducing Pt and Ir precursors onto Au nanoparticles in an aqueous solution at a temperature near to boiling. This method was chosen to promote the formation of a well-mixed atomic layer of Pt and Ir on Au nanoparticles. The molar ratio of metals was 10:1:1 for Au:Pt:Ir based on an estimated one monolayer coverage of Pt and Ir on 5-nm Au particles. As shown in Figure 1a, the resulting Au@PtIr core-shell nanoparticles exhibit X-ray diffraction peaks at the positions close to those for face-centered-cubic Au, indicating that the Pt and Ir atoms are in registry with the underlying Au lattice (a_{Au} = 0.408 nm). The tensile strains calculated from the peak positions are 3.8% relative to Pt (a_{Pt} = 0.392 nm) and 6.1% relative to Ir (a_{Ir} = 0.386 nm). These values are close to the lattice mismatches of 4.1% and 6.3%, respectively. In contrast, the lattice spacing of PtIr alloy particles is between those of Pt and Ir, resulting in tensile strained Ir but compressively strained Pt.

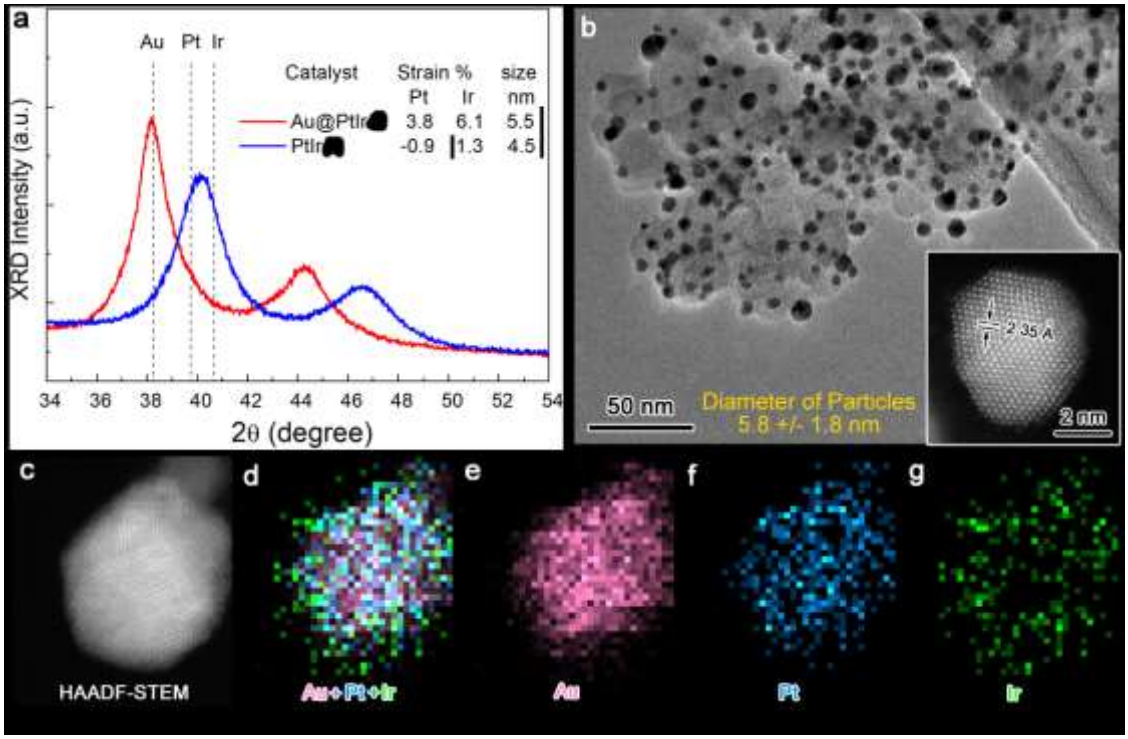

Figure 1. (a) X-ray diffraction profile of Au@PtIr/C compared to PtIr/C showing Au-induced lattice expansion. (b) TEM image of well dispersed Au@PtIr particles on carbon support with narrow particles size distribution. The insert shows atomic spacing of 2.35 Å consistent with the spacing between Au{111} planes. (c-g) HAADF-STEM image and two-dimensional mapping of Au-Lα (pink), Pt-Lα (blue), and Ir-Lα (green) EDS intensities for a typical Au@PtIr particle.

The transmission electron microscopy (TEM) images shown in Figure 1b verifies a narrow particle size distribution of ±1.8 nm and a lattice spacing of Au {111} facets. Note that the surface to core atomic ratio for 5.8 ±1.8 nm particles calculated using a cuboctahedra model is 0.19 and the molar ratio of 10:1:0.7 for Au:Pt:Ir determined by x-ray absorption spectroscopy yields a 0.17 (Pt+Ir) to Au ratio. Thus, the PtIr shell is essentially in the form of monoatomic islands. Figures 1c-f show the elemental distribution of a representative Au@PtIr particle. The 2D images of energy dispersive spectroscopy (EDS) mapping show that the signals for Pt (blue) and Ir (green) spread evenly, much less intense in the center compared to that of Au (pink), which indicates that Pt and Ir form a thin shell on the Au core. The Pt signal covers similar area in the image as the Au signal indicating that Pt atoms are mainly in the first atomic layer on Au. The Ir signal spreads to a slightly larger area compared to the Pt and Au signals suggesting that Ir atoms are partly in the

first adlayer mixing with Pt and partly on top of that adlayer. Thus, the thin PtIr shell is rich of atomic steps.

Catalyst performance for EOR in alkaline solutions. Figure 2a shows an EOR peak current of 58 A mg^{-1} PGM obtained using the Au@PtIr/C catalyst in 1 M ethanol and 1 M KOH solution, which is 8 and 38 times of the peak currents on Au@Pt/C and Au@Ir/C, respectively. On single crystal surfaces, the EOR peak current on Pt(111) is about fivefold of that on Ir(111), while the EOR onset potential is lower on Ir(111) than on Pt(111) by about 0.25 V.[25] This trend persists for the Au@Pt/C and Au@Ir/C catalysts as shown by the blue and green curves in Figure 2a. It is remarkable that the combination of Pt and Ir on Au results in an eightfold increase in peak current and a 0.25 V reduction of onset potential compared to Au@Pt/C. To compare with a not-core-shell structured PtIr/C catalyst (1:1 atomic ratio, similar particle size), Figure 2b shows the EOR currents normalized to the mass of all metals. The Au@PtIr/C catalyst exhibited 0.52 A mg^{-1} at 0.6 V, 4.3 times of that on PtIr/C, demonstrating a large activity enhancement due to the Au cores. These measurements were carried out using gas diffusion electrodes, focusing on the EOR performance below 700 mV where the activity matters the most for fuel cell applications. The high and reversible EOR current up to 700 mV on Au@PtIr indicates its promise as a practical anode catalyst for direct liquid fuel cells operating at the ambient temperature.

Further enhancement of EOR current at low potentials was obtained by adding acid-treated functional carbon nanotubes (f-CNT) on the gas diffusion layer before loading Au@PtIr/C catalyst. Figure 2c shows that the presence of f-CNT lowers the onset potential for EOR and increases the EOR currents at potentials below 0.55 V. At 0.45 V, the EOR current doubles that in the absence of f-CNT. The f-CNT most likely enhances OH^- transport, which is important for dehydrogenation at low potentials as it is suggested that the first step of dehydrogenation is catalyzed by base.[18] As oxidation becomes more dominant than dehydrogenation at higher potentials, the advantage of f-CNT diminishes. A similar effect of carbon materials on enhancement of EOR performance in base was shown on Pd-based catalysts in the previous studies.[11,26] This differs from EOR in acid, where metal oxides are more effective than carbon materials for enhancing EOR activity at low potentials.[6]

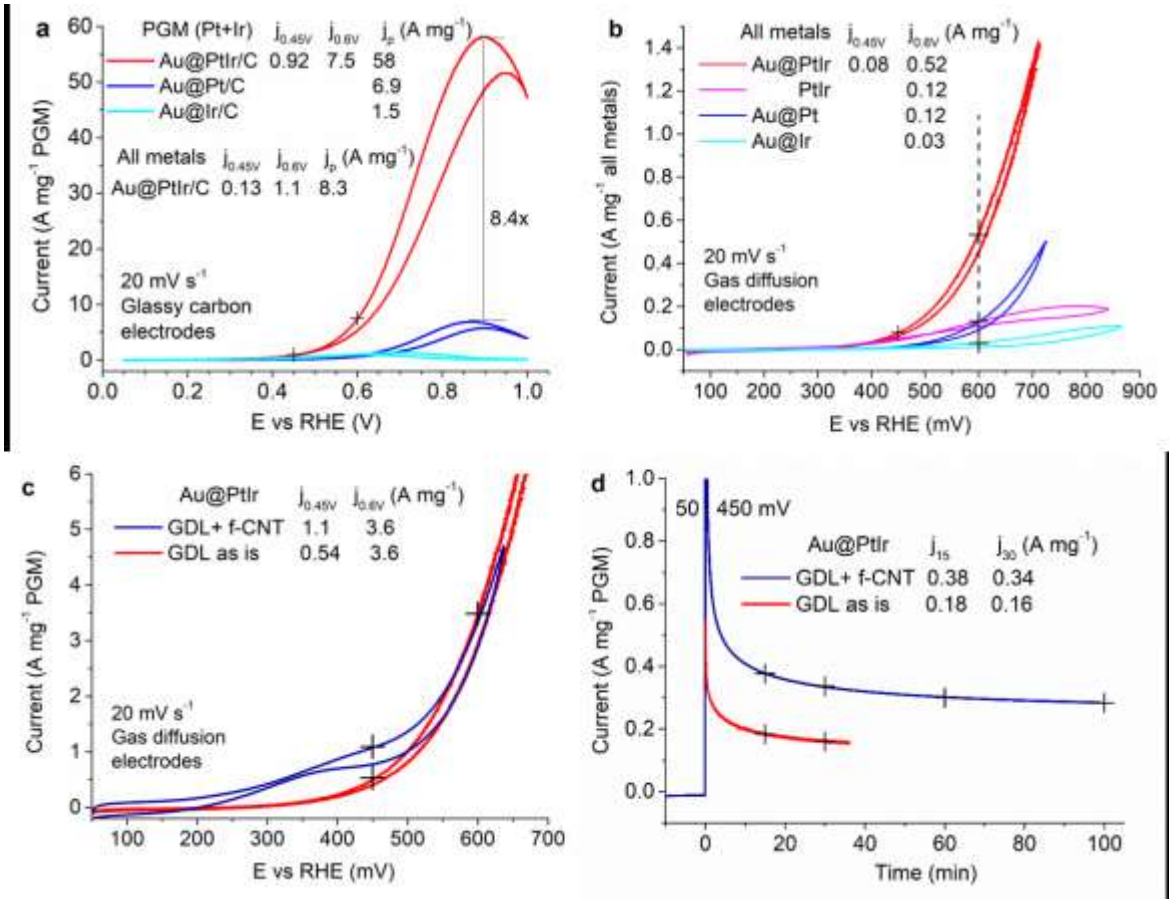

Figure 2. EOR performance of Au@PtIr/C compared with Au@Pt/C, Au@Ir/C, and PtIr/C in 1 M ethanol and 1 M KOH. (a) PGM mass activities of three Au core catalysts. (b) All metal mass activities of the three core-shell catalysts and a PtIr (1:1 molar ratio) alloy catalyst. (c) PGM mass activities of Au@PtIr without and with functional carbon nanotube (f-CNT) on gas diffusion electrodes. (d) Durability measured by chronoamperometry at 0.45 V versus RHE.

Figure 2d shows the chronoamperometry curves measured at 0.45 V after stepping potential from 0.05 V for the Au@PtIr catalysts with and without f-CNT. After 15 minutes, the coverage of various EOR intermediates likely reached a quasi-steady state as the currents start to level off. The currents of 0.38 and 0.18 A mg^{-1} at 15 minute for the Au@PtIr catalysts with and without f-CNT, respectively, are an order of magnitude higher than those for Pd/C (~0.03 A mg^{-1}) and Pt/C (~0.01 A mg^{-1}).[27] Furthermore, the EOR current retained above 0.28 A mg^{-1} after 100 minutes. This outstanding sustainable EOR activity at 0.45 V suggests the absence of poisoning intermediate on the Au@PtIr catalyst, which is supported by the IRRAS results described in next subsection.

Table 1. PGM activities of most active EOR catalysts in selected categories

Catalyst	$J_{0.45V\ 30\ min}$ A mg^{-1}	$J_{0.45V}$ A mg^{-1}	$J_{0.6V}$ A mg^{-1}	J_{peak} A mg^{-1}	Rate* mV s^{-1}	Year of Reference
1 M KOH, 1 M ethanol						
$Au_{10}@Pt_1Ir_{0.7}$		0.92 **(**0.13**)****	7.5 (1.1)	58 (8.3)	20	This work
$Au_{10}@Pt_1Ir_{0.7}$/f-CNT-GDE	0.34	1.10 (0.16)	3.6 (0.52)		20	This work
$Au_{10}@Pt_1Ir_{0.7}$/GDE,	0.16	0.54 (0.08)	3.6 (0.52)		20	This work
$Pt_4Au_5Ir_1$ alloy		~0.07***	~.018	0.05	10	2017[17]
Pt_1Au_1 alloy		~0.07	~.017	0.048	10	2014[28]
$Pt_{54}Rh_4Cu_{42}$		~0.7	~2	4.09	50	2018[15]
Pt_2Rh				~1.8	50	2010[16]
Pt_1Rh_3 nanodendrites		~0.11	~0.42	0.462	50	2018[29]
Pt [15 min at 0.45 V] ****	0.01	0.045	~0.42	~0.8	10	2012[27]
Pd [15 min at 0.45 V]	0.03	0.068	~0.40	~2.3	10	2012[27]
PdAuAg aerogel		~3 (~1.5)	~7.8 (~3.4)	~40 (21)	50	2017[8]
Pd aerogel		~0.4	~2.9	7.83	50	2012[30]
Pd aerogel [0.5M ethanol]		~0.6	~1.4	4.70	20	2018[31]
Pd-CNTs		~0.2	~1	~4.9	50	2018[26]
$Pd_{40}Ni_{43}P_{17}$			~1	4.95	100	2017[10]
PdRu-NiZn oxyphosphide				4.72	50	2018[32]
Ni@Au@Pd/rGO [2M KOH]	~0.04			~3 (~2)	50	2018[11]
$Pd_{30}Pt_{29}Au_{41}$-Ppy				~8 (~6)	50	2017[9]
PdPt [0.5 M NaOH]				5.8	50	2015[33]
$Pd@Pt_3Ni$		~0.35	~1.5	5.78	50	2018[12]
0.1 M $HClO_4$ 0.5 M ethanol						
Pt_3Rh_1/SnO_2	~0.17	~0.7	~1.2	1.5	10	2013[6]
Pt_3RhSn	~0.01	0.031	~0.083		20	2018[34]
Pt_1Rh_3 nanodentrites			~0.02	0.23	50	2018[29]

* Activities determined by polarization curves are usually lower with lower potential sweep rate.
** Values in ( ) are mass activities of precious metals including PGM, Au, and Ag.
*** Values with ~ in front were obtained either by reading from plots or involving a conversion made with metal loadings or reference electrode.
**** Notes in [ ] are the measurement conditions, which differ from that commonly used.

Table 1 summaries the PGM activities of the Au@PtIr core-shell catalyst and the most active EOR catalysts of various types previously reported. The peak current in forward potential sweep given in the fifth column is commonly used for comparing catalyst performance. In most cases, the peak potentials are above 0.7 V, out of the overpotential range for an anode in fuel cells. Thus, activities at 0.45 and 0.6 V are listed in the third and fourth columns, respectively. The second

column provides the EOR activity after 30 min at 0.45 V. As the list shown, Pd-based[8,10,11,13,14,30,31] and PdPt-based[7,9,12] catalysts performed better than Pt-based[15–17,28,29] catalysts prior to this work for EOR in alkaline solutions. Different from EOR in acid, where Rh and Sn oxide greatly promoted the activity on Pt,[5,35] Au is involved in the most active Pt-based (this work) and Pd-based[8] catalysts for EOR in alkaline solutions. It is highly remarkable that the activity enhancement factor is over 1000 for the Au@PtIr core-shell catalyst (this work) as compared to AuPtIr alloy particles.[17]

In-situ IRRAS and active reaction pathways. To gain insights into how metal composition and atomic structure affect EOR selectivity toward C1-12e pathway, onset potential, and peak current, we performed *in-situ* IRRAS studies of EOR in 1 M KOH on the ternary Au@PtIr core-shell catalyst and its two binary subsets: PtIr alloy and Au@Pt core-shell catalysts. For EOR in acid, the appearance of the 2343 cm^{-1} CO_2 band indicates the formation of C1-12e product.[5,20] In alkaline solutions, CO_2 reacts with OH^- to form carbonate and the CO_2 band appears only when pH is ≤13.[21] Figure 3a shows the spectra acquired during a positive potential sweep for Au@PtIr/C, in which the 2343 cm^{-1} CO_2 band emerges at potentials above 0.8 V. This feature indicates that the C1-12e pathway is active on the ternary catalyst and that the pH in the thin layer solution between electrode and optical window can be lowered significantly by EOR during the time for a potential scan at 1 mV s^{-1} from 0.05 V to 0.8 V.

To evaluate selectivity between C1-12e and C2-4e pathways at low potentials, we analyzed the characteristic bands for carbonate and acetate. In transmission spectra, a single band at 1390 cm^{-1} was observed for Na_2CO_3 while CH_3COONa exhibited two bands at 1550 and 1415 cm^{-1} plus a narrow and weak band at 1348 cm^{-1}.[22] As illustrated in Figure 3b, fitting the top spectrum (908 mV) with three Lorentzian peaks deconvolutes the overlapped bands in the region from 1430 to 1260 cm^{-1}. The areas under the 1408 and 1394 peaks are taken as the integrated absorbance for CH_3COO^- and HCO_3^-/CO_3^{2-}, respectively. The third fitted peak at 1346 cm^{-1} is broad, differing from the narrow 1348 cm^{-1} band from acetate (ignored in fitting), and is likely due to the formation of small amount of $HCOO^-$. This is supported by the assignment of 1340 cm^{-1} to adsorbed formate on Pt(111).[36] Other characteristic bands include a small band at 923 cm^{-1} for acetaldehyde,[37] a bipolar band at 1044 cm^{-1} due to adsorbed ethanol,[37,38] and a band that shifts from 1956 to 1985 cm^{-1} with increasing potential (Figure 3c), which is assigned to linearly adsorbed CO.[39]

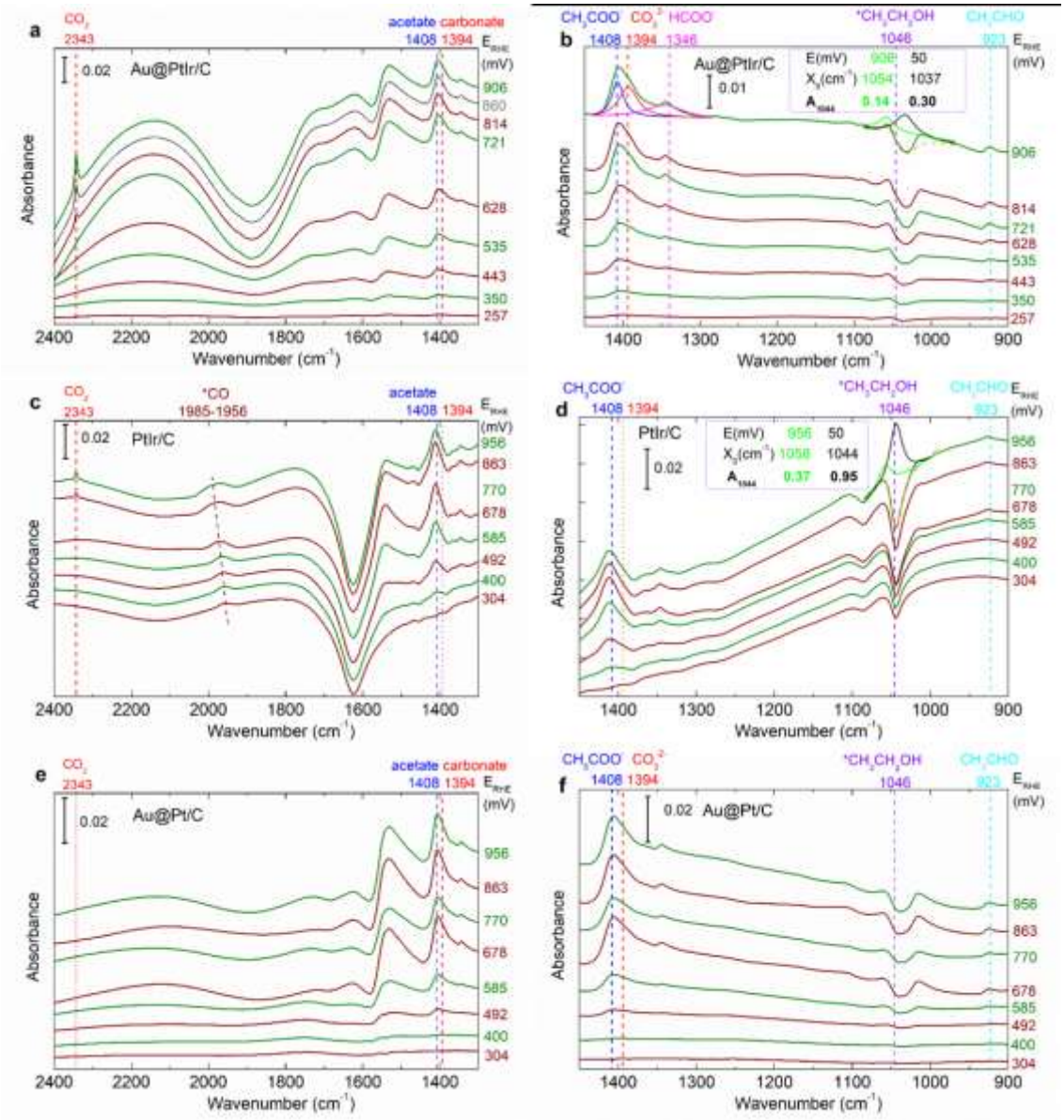

Figure 3. *In-situ* IRRAS spectra for EOR on Au@PtIr/C (a,b), PtIr/C (c,d), and Au@Pt/C (e,f) in 1 M KOH and 1 M ethanol solution, potential sweep rate 1 mV s^{-1}, reference spectrum at 50 mV. An example of deconvoluted bands (blue, red, pink) in the region 1440-1260 cm^{-1} region is shown in (b). The fits (dashed orange curve = green curve – black curve) to the data (dark green) for the 1046 cm^{-1} band are shown in (b) and (d) with the integrated absorbances listed in dashed box. Adsorbed species are marked by * and their IR bands shifted with potentials.

The integrated absorbance values for different EOR products on Au@PtIr are plotted as a function of potential in Figure 4a. The rising absorbance values for acetate (circles) and carbonate

(triangles) reflect the concentration increases for C2-4e and C1-12e products, respectively. To determine the selectivity toward C1-12e pathway at potentials below 0.7 V, we calculated the ratio for the charges generated from forming carbonate and acetate from the ratio of absorbance values using $C_{Carbonate}/C_{Acetate} = 6A_{1394} / 4A_{1408} / 2.2$, in which 6 and 4 are the electron transfer numbers per carbonate and acetate, respectively; 2.2 is the absorbance coefficient ratio determined by measuring absorbance ratio for a solution containing equal molar amounts of carbonate and acetate. As shown in Figure 4a (right axis), the $C_{Carbonate}/C_{Acetate}$ ratio is about 1.3 between 0.3 and 0.6 V for Au@PtIr/C. Since the band at 1348 cm^{-1} for $HCOO^-$ (a C1-10e product) and the 923 cm^{-1} band CH_3CHO (a C2-2e product) are weak, the percentage of current generated by C1 pathway can be estimated by counting the charges associated with the two major products, i.e., $C_{Carbonate} /(C_{Carbonate} + C_{Acetate}) = 1.3/(1.3+1) = 0.57$. Thus, about 57% EOR current is generated via a direct C1-12e pathway on Au@PtIr/C.

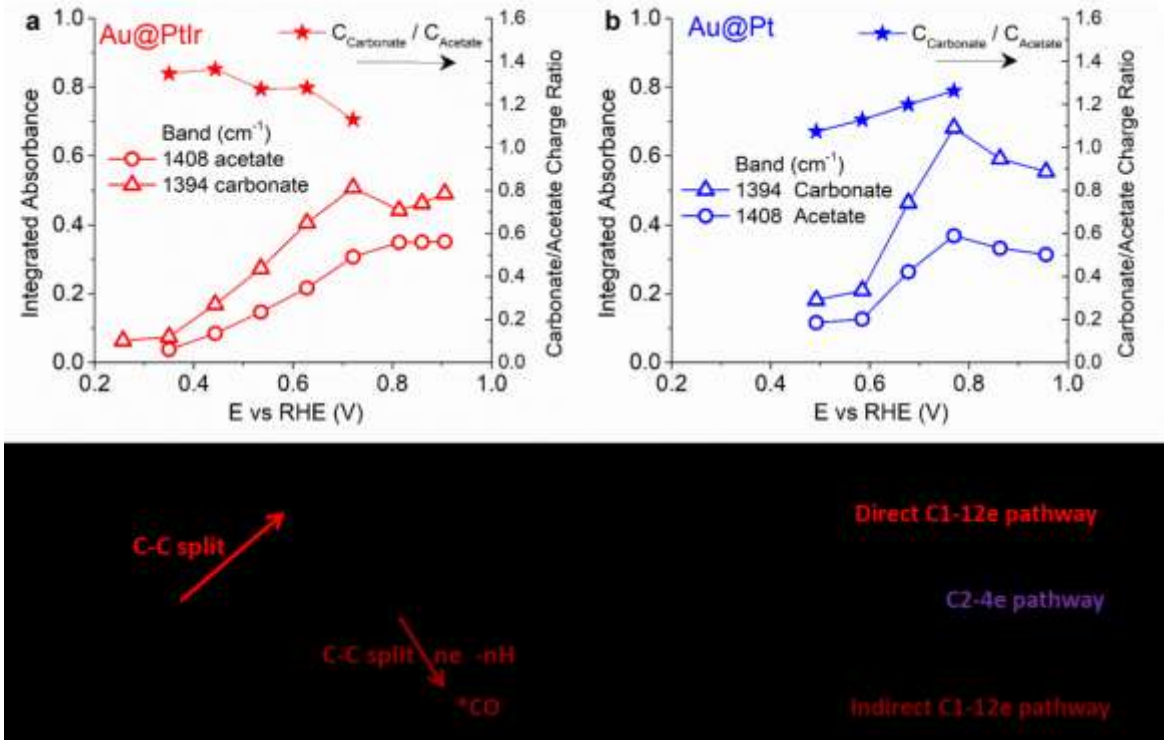

Figure 4. (a,b) Integrated absorbances of EOR products (Left axis) and molar ratio of carbonate to acetate (Right axis) for Au@PtIr/C (a) and Au@Pt/C (b) catalysts. (c) Scheme of three active EOR pathways.

As shown by the scheme in Figure 4c, the direct C1-12e pathway is characterized by the C-C bond splitting via ethanol dissociative adsorption, resulting in hydrogen-rich C1 fragments that are fully oxidized without poisoning intermediates. This pathway competes with non-dissociative adsorption of ethanol, which can then be dehydrogenated without or with C-C bond splitting. The former leads to the C2-4e pathway and the latter is termed as indirect C1-12e pathway, in which the C-C bond splits after partial dehydrogenation and has adsorbed CO as a major intermediate.

Interestedly, the direct C1-12e pathway is also activated on Au@Pt/C, while PtIr/C provides an example of active indirect C1-12e pathway. Figure 4b shows that the $C_{Carbonate}/C_{Acetate}$ ratio (right axis) measured for Au@Pt/C is between 1.1 and 1.3, close to that for Au@PtIr. In contrast, this ratio is zero (not shown) for EOR on PtIr/C because there is no measurable absorbance for carbonate as the peaks centered at 1411 cm^{-1} in Figure 3d are symmetric without a shoulder at 1394 cm^{-1}. The appearance of the ~1970 cm^{-1} band for adsorbed *CO (Figure 3c) and its growth with increasing potential (pink cross in Figure 4b) concurs with the lack of carbonate, indicating that oxidation of strongly adsorbed CO is the rate-limiting step for complete ethanol oxidation below 0.8 V on PtIr/C.

The evidence of the link between non-dissociative ethanol adsorption and formation of strongly adsorbed *CO can be found by the larger bipolar band at 1046 cm^{-1} for PtIr/C (Figure 3d) than for Au@PrIt/C (Figure 3b) and Au@Pt/C (Figure 3f). A bipolar band arises from the peak position difference between the spectrum obtained at a high potential and the reference spectrum.[40] The downward peak shows decreasing coverage of adsorbed ethanol with increasing potential from the reference potential of 0.05 V and a small upward peak emerges due to a potential-induced shift of the band center. For the spectra at the highest potential in Figures 3b and 3d, we show that the bipolar band can be replicated by the orange curve obtained by subtracting the black curve, $A(_{50mV})$ from the green curve $A(_{E})$. The integrated absorbance values (given in the inserts) are higher at both low and high potentials for PtIr/C than those for Au@PtIr/C.

Structural and compositional effects on EOR specific activity. Figures 5a and 5b summarize the voltammetry and EOR peak currents normalized to the calculated metal surface area. Hydrogen adsorption is significantly stronger on PtIr/C than the core-shell catalysts with Au as the cores. The bars in Figure 5b show EOR peak currents versus peak potential. Results for EOR on (111) single crystals of Ir, Pt and Au[7] are included to show the property of metals without

nanostructure-induced effect. Nanometer-sized particles have many low-coordination sites at the edges, which can be highly active for many reactions. For example, a 4.5 nm cuboctahedron Au particle has about 10 atoms at each of 24 edges, which account for ~20% surface atoms. While there is no EOR current below 0.9 V on Au(111) single crystal surface,[25] EOR current was observed on Au nanoparticles at potentials comparable to that of Pt nanoparticles.[28] For EOR in acid, the CO_2 band at 2343 cm^{-1} was observed for Pt monolayer and sub-monolayer on Au nanoparticles,[20] but not for Pt monolayer on Au(111) single crystals.[41] Thus, ethanol dissociation is likely facile at the monoatomic steps of Pt or PtIr islands, especially those near the edges of Au nanoparticles.

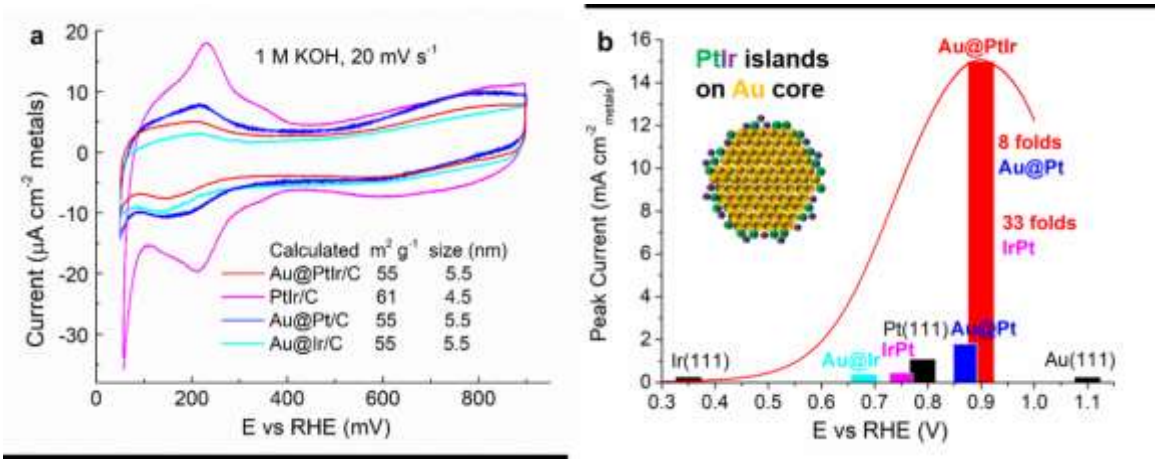

Figure 5. (a) Voltammetry curves normalized to metal surface areas calculated from average metal densities and diameter of particles, using mass-specific surface area = 6000/diameter/density. (b) Area-specific peak current versus peak potential (bars) for EOR in 1 M KOH and 1 M ethanol on Au@Ir/C (light blue), PtIr/C (pink), Au@Pt/C (blue), and Au@PtIr/C (red) catalysts. Red curve is an EOR polarization curve for Au@PtIr/C. Values for unary Ir, Pt, and Au (black bars) are referred to the results on (111) surfaces reported in literature.[42] Insert: schematic model of the cross-section of a Au@PtIr particle.

Gold cores induce a lateral lattice expansion of Pt and Ir monolayers. The tensile strain has been shown highly effective in enhancing EOR current in acid, especially at high potentials. Relative to Pt(111), Pt monolayer on Au(111) exhibits a fourfold peak current, while Pt monolayers on Pd(111), Ir(111), Rh(111), and Ru(0001) are compressed and thus result in lower peak currents than that on Pt(111).[41] The effect on peak current is even higher for methanol

oxidation reaction as a sevenfold enhancement is seen on Pt monolayer/Au(111) relative to Pt(111).[41] Thus, oxidation of either C1 or C2 intermediates are benefited from the Au-induced tensile strain that enhances water and OH adsorption in acid and base, respectively. In this study, the three orders of magnitude higher EOR activity on Au@PtIr core-shell catalysts than on AuPtIr alloy catalysts[17] demonstrates the importance of both the atomic steps for promoting direct C1 pathway and the tensile strain for improving oxidation kinetics.

Iridium, on the other hand, acts as a promotor for dehydrogenation, which lowers the onset potential. For example, the ammonia oxidation reaction, $2NH_3 + 6OH^- = N_2 + 6H_2O + 6e^-$, involves dehydrogenation but not an oxidation process. Density functional theory (DFT) calculations have found Ir as the best metal for dehydrogenation of ammonia,[43] and experimental studies have shown the importance of Ir for lowering the onset potential for ammonia oxidation.[44] For EOR in base, the onset potential for producing carbonate/acetate is in the order of Au@PtIr < PtIr < Au@Pt (Figures 4a and 4b), supporting dehydrogenation as the rate limiting step at low potentials for EOR and Ir being a dehydrogenation promotor. In addition, DFT calculations have found that Ir has the highest barrier for forming CH_3COOH from CH_3CO + OH and the lowest barrier for C-C bond cleavage in CHCO to form CH + CO species among Pd, Pt and Ir.[45] Thus, Ir makes the indirect C1-12e pathway more favorable than the C2-4e pathway. For completing the indirect C1-12e pathway, Au-induced tensile strain is important for oxidation of strongly adsorbed *CO, and thus, Ir and Au core together promote complete ethanol oxidation at higher potentials. The 8- and 33-fold activity enhancement over Au@Pt and PtIr, respectively, demonstrate the impact of the synergy generated from three activity promoting aspects: monoatomic steps for ethanol dissociation, Ir for dehydrogenation, and Au-core-induced tensile strain for oxidation.

In summary, the ternary core-shell catalyst, Au@PtIr/C, exhibits extraordinary EOR performance in alkaline solution – a high peak current of 58 A mg^{-1} (PGM) and 8.3 A g^{-1} (all metals), a low onset potential of 0.3 V, and a high percentage C1-12e current of 57%. Three orders of magnitude activity enhancement with respect to AuPtIr alloy particles illustrate a remarkable structural sensitivity of EOR kinetics and the effectiveness in activating a direct C1-12e pathway. Lattice expansion induced by Au cores and atomic steps of PtIr monolayer islands on Au activate a direct C1-12e EOR pathway by promoting ethanol dissociative adsorption at low potentials. The resulting hydrogen-rich single carbon fragments can be fully oxidized without generating strongly adsorbed CO, and thus, a hurdle for complete full oxidation of ethanol at low potentials is

circumvented. Adding Ir at the surface with Au as the core allows them to play complementary roles in promoting dehydrogenation and oxidation reaction steps, respectively. The results are encouraging to further advance anode catalysts for direct liquid fuel cells and the new insights can guide rational design of multi-component and nanostructured catalysts for electrooxidation of small organic molecules.

EXPERIMENTAL SECTION

Chemicals and materials. All metal precursors, $HAuCl_3 \cdot H_2O$, $IrCl_3 \cdot H_2O$, and K_2PtCl_4 purchased from Sigma-Aldrich were used without further purifications. Vulcan 72R was used as the carbon support.

Synthesis of 20 wt.% Au/C. The 20 wt.% Au/C was synthesized by the reduction of Au precursor using sodium borohydride, followed by the loading to the carbon support. In a typical synthesis, 2 mL of 1 wt.% $HAuCl_3 \cdot H_2O$ aqueous solution and 2 mL of 1 wt.% trisodium citrate aqueous solution were added to 200 mL of water in a round bottom flask. One minute after the solution mixing, 2 mL of 0.075 wt.% sodium borohydride in 1 wt.% trisodium citrate solution was added to the reaction solution under vigorous stirring. After another 5 min, 40 mg of carbon black were added to the solution. The reaction proceeded under vigorous stirring for additional 2 h. The product was purified by water twice and ethanol once, collected by vacuum filtration, and dried under vacuum overnight for further use.

Synthesis of Ir on 20 wt.% Au/C. The Ir on 20 wt.% Au/C was synthesized by the reduction of Ir precursor using ascorbic acid at in the presence of 20 wt.% Au/C. In a typical synthesis, 60 mg of ascorbic acid and 50 mg of Au/C (20 wt.%) was added to 10 mL of water in a 100 mL round bottom flask. After the mixture in water was heated boiled, 6 mL of 0.5 mg/mL $IrCl_3 \cdot H_2O$ aqueous solution was added to the mixture at a rate a rate of 2.0 mL/h. After the addition of Ir precursor, the reaction proceeded under vigorous stirring for additional 2 h to overnight. The product was purified by water twice and ethanol once, collected by vacuum filtration, and dried under vacuum overnight for further use.

Synthesis of Pt and Ir on 20 wt.% Au/C in water. The Pt-Ir shell on 20 wt.% Au/C core was synthesized by the reduction of Pt and Ir precursors using ascorbic acid at in the presence of 20 wt.% Au/C. In a typical synthesis, 60 mg of ascorbic acid and 50 mg of Au/C was added to 10 mL of water in a 100 mL round bottom flask. After the mixture in water was heated to boil, 3 mL of

0.5 mg/mL $IrCl_3 \cdot H_2O$ and 3 mL of 0.7 mg/mL K_2PtCl_4 aqueous solutions were simultaneously added to the mixture at a rate of 2.0 mL/h. After the addition of Pt and Ir precursors, the reaction proceeded under vigorous stirring for additional 2 h to overnight. The product was purified by water twice and ethanol once, collected by vacuum filtration, and dried under vacuum. The molar ratio determined by XAS for Au:Pt:Ir is 10:1:0.7 (within <5% error), close to that of the precursors.

Characterization. X-ray diffraction (XRD) profiles of catalyst samples were collected using Cu Kα radiation (λ = 1.5418 Å). Transmission electron microscopy (TEM) images were obtained using a JEOL JEM-ARM200CF operated at 200 kV.

Catalyst ink and electrode preparation Catalyst inks were made with a mixed solvent of deionized water, ethanol, and isopropanol (volume ratio 1:1:2) containing Nafion with 0.1 to 0.3 weight ratio to the carbon weight in the catalyst. After sonicating in ice water bath for more than 20 min, 5 to 15 μL of catalyst ink was dropped onto glassy carbon electrode to have a catalyst loading of 0.1 mg cm^{-2}. The total metal loadings were about 0.02 mg cm^{-2}. For gas diffusion electrode samples, a calculated amount of ink was placed over 1 cm^2 area at one end of a 1.4 cm wide and 3 cm long gas diffusion layer (Sigracet 25 BC) to get total metal loading about 0.1 mg cm^{-2}.

Electrochemical measurements. A Voltalab PGZ 402 potentiostat was used for electrochemical measurement with a Hg/HgO electrode as the reference electrode and a Pt-flag as the counter electrode in 1 M KOH solution. The zero potential versus reversible hydrogen electrode (RHE) in 1 M KOH was determined by the open circuit potential on Pt in hydrogen saturated solution. The iR-free potential was obtained by subtracting the product of measured currents and the high-frequency resistance determined from electrochemical impedance spectra acquired at 500 mV versus RHE.

In-situ infrared reflection absorption spectroscopy (IRRAS). In-situ IRRAS measurements were carried out with a Nicolet iS50 FT-IR spectrometer equipped with an A-type MCT detector cooled with liquid nitrogen. The working electrodes were made via casting appropriate amounts of catalyst inks on a gold disk electrode. The loadings of carbon supported catalysts are ~0.05 mg cm^{-2} total metals. A Hg/HgO electrode was used as the reference electrode and Pt was the counter electrode. During in situ IRRAS measurements, the working electrode was pressed against the flat surface of a ZnSe hemisphere. The spectral resolution was set at 4 cm^{-1} and the reference reflectivity (R_{ref}) was taken at 50 mV vs. RHE. Absorbance spectra, $-\log(R/R_{ref})$, are presented.

Each of potential-dependent spectra was acquired by integrating 288 interferograms collected in 50 s. The potential for each spectrum is the average potential between that at the beginning and the end of data collection while the potential was continuously increased at 1 mV s^{-1}.

AUTHOR INFORMATION

Corresponding Authors

*chenj@uark.edu

*jia@bnl.gov

ORCID

Liang Song: 0000-0002-4740-4075

Yimei Zhu: 0000-0002-1638-7217

Radoslav R. Adzic: 0000-0002-9387-8618

Jingyi Chen: 0000-0003-0012-9640

Jia X. Wang: 0000-0002-3947-9296

Notes

The authors declare no competing financial interest.

ACKNOWLEDGMENT

This research at Brookhaven National Laboratory was supported by the U.S. Department of Energy, Office of Science, Office of Basic Energy Sciences, Chemical Sciences, Geosciences and Biosciences Division under contract DE-SC0012704. The research used 8-ID (ISS) beamline of the National Synchrotron Light Source II and the Center for Functional Nanomaterials, U.S. Department of Energy (DOE) Office of Science User Facilities operated for the DOE Office of Science by Brookhaven National Laboratory under Contract No. DE-SC0012704. J.C. gratefully acknowledges funding support from the National Science Foundation, Division of Chemical, Bioengineering, Environmental and Transport Systems (CBET) Catalysis program (Award # 1703827).

REFERENCES

(1) Kamarudin, M. Z. F.; Kamarudin, S. K.; Masdar, M. S.; Daud, W. R. W. *Int. J. Hydrogen Energy* **2013**, *38* (22), 9438–9453.

(2) An, L.; Zhao, T. S.; Li, Y. S. *Renew. Sustain. Energy Rev.* **2015**, *50*, 1462–1468.

(3) Zakaria, Z.; Kamarudin, S. K.; Timmiati, S. N. *Appl. Energy* **2016**, *163*, 334–342.

(4) Wang, Y.; Zou, S.; Cai, W.-B. *Catalysts* **2015**, *5* (3), 1507–1534.

(5) Kowal, A.; Li, M.; Shao, M.; Sasaki, K.; Vukmirovic, M. B.; Zhang, J.; Marinkovic, N. S.; Liu, P.; Frenkel, A. I.; Adzic, R. R. *Nat. Mater.* **2009**, *8* (4), 325–330.

(6) Li, M.; Cullen, D. A.; Sasaki, K.; Marinkovic, N. S.; More, K.; Adzic, R. R. *J. Am. Chem. Soc.* **2013**, *135* (1), 132–141.

(7) Pan, Y.; Guo, X.; Li, M.; Liang, Y.; Wu, Y.; Wen, Y.; Yang, H. *Electrochim. Acta* **2015**, *159*, 40–45.

(8) Nahar, L.; Farghaly, A. A.; Esteves, R. J. A.; Arachchige, I. U. *Chem. Mater.* **2017**, *29* (18), 7704–7715.

(9) Ghosh, S.; Bera, S.; Bysakh, S.; Basu, R. N. *ACS Appl. Mater. Interfaces* **2017**, *9* (39), 33775–33790.

(10) Chen, L.; Lu, L.; Zhu, H.; Chen, Y.; Huang, Y.; Li, Y.; Wang, L. *Nat. Commun.* **2017**, *8*, 1–9.

(11) Wang, F.; Qiao, J.; Wang, J.; Wu, H.; Yue, X.; Wang, Z.; Sun, W.; Sun, K. *Electrochim. Acta* **2018**, *271*, 1–9.

(12) Wang, Y.; Wang, W.; Xue, F.; Cheng, Y.; Liu, K.; Zhang, Q.; Liu, M.; Xie, S. *Chem. Commun.* **2018**, *54* (41), 5185–5188.

(13) Zareie Yazdan-Abad, M.; Noroozifar, M.; Alfi, N.; Modarresi-Alam, A. R.; Saravani, H. *Int. J. Hydrogen Energy* **2018**, *43* (27), 12103–12109.

(14) Xu, H.; Song, P.; Zhang, Y.; Du, Y. *Nanoscale* **2018**, *10* (26), 12605–12611.

(15) Han, S.; Liu, H.; Chen, P.; Jiang, J.; Chen, Y. *Adv. Energy Mater.* **2018**, *8* (24), 1–10.

(16) Shen, S. Y.; Zhao, T. S.; Xu, J. B. *Int. J. Hydrogen Energy* **2010**, *35* (23), 12911–12917.

(17) da Silva, S. G.; Fontes, E. H.; Assumpção, M. H. M. T.; Linardi, M.; Spinacé, E.; Silva, J. C. M.; Neto, A. O. *Ionics (Kiel).* **2017**, *23* (9), 2367–2376.

(18) Kwon, Y.; Lai, S. C. S.; Rodriguez, P.; Koper, M. T. M. *J. Am. Chem. Soc.* **2011**, *133* (18), 6914–6917.

(19) Rizo, R.; Arán-Ais, R. M.; Padgett, E.; Muller, D. A.; Lázaro, M. J.; Solla-Gullón, J.; Feliu, J. M.; Pastor, E.; Abruña, H. D. *J. Am. Chem. Soc.* **2018**, *140* (10), 3791–3797.

(20) Loukrakpam, R.; Yuan, Q.; Petkov, V.; Gan, L.; Rudi, S.; Yang, R.; Huang, Y.; Brankovic, S. R.; Strasser, P. *Phys. Chem. Chem. Phys.* **2014**, *16* (35), 18866–18876.

(21) Fang, X.; Wang, L.; Shen, P. K.; Cui, G.; Bianchini, C. *J. Power Sources* **2010**, *195* (5), 1375–1378.

(22) Zhou, Z. Y.; Wang, Q.; Lin, J. L.; Tian, N.; Sun, S. G. *Electrochim. Acta* **2010**, *55* (27), 7995–7999.

(23) Buso-Rogero, C.; Brimaud, S.; Solla-Gullon, J.; Vidal-Iglesias, F. J.; Herrero, E.; Behm, R. J.; Feliu, J. M. *J. Electroanal. Chem.* **2016**, *763*, 116–124.

(24) Huang, L.; Sorte, E. G.; Sun, S. G.; Tong, Y. Y. J. *Chem. Commun.* **2015**, *51* (38), 8086–8088.

(25) Lopes, P. P.; Strmcnik, D.; Jirkovsky, J. S.; Connell, J. G.; Stamenkovic, V.; Markovic, N. *Catal. Today* **2015**, *262*, 41–47.

(26) Zareie Yazdan-Abad, M.; Noroozifar, M.; Alfi, N.; Modarresi-Alam, A. R.; Saravani, H. *Int. J. Hydrogen Energy* **2018**, *43* (27), 12103–12109.

(27) Ma, L.; Chu, D.; Chen, R. *Int. J. Hydrogen Energy* **2012**, *37* (15), 11185–11194.

(28) Da Silva, S. G.; Silva, J. C. M.; Buzzo, G. S.; De Souza, R. F. B.; Spinacé, E. V.; Neto, A. O.; Assumpção, M. H. M. T. *Int. J. Hydrogen Energy* **2014**, *39* (19), 10121–10127.

(29) Bai, J.; Xiao, X.; Xue, Y. Y.; Jiang, J. X.; Zeng, J. H.; Li, X. F.; Chen, Y. *ACS Appl. Mater. Interfaces* **2018**, *10* (23), 19755–19763.

(30) Liu, W.; Herrmann, A. K.; Geiger, D.; Borchardt, L.; Simon, F.; Kaskel, S.; Gaponik, N.;

Eychmüller, A. *Angew. Chemie - Int. Ed.* **2012**, *51* (23), 5743–5747.

(31) Shafaei Douk, A.; Saravani, H.; Noroozifar, M. *Electrochim. Acta* **2018**, *275*, 182–191.

(32) Xu, H.; Song, P.; Zhang, Y.; Du, Y. *Nanoscale* **2018**, *10* (26), 12605–12611.

(33) Pan, Y.; Guo, X.; Li, M.; Liang, Y.; Wu, Y.; Wen, Y.; Yang, H. *Electrochim. Acta* **2015**, *159*, 40–45.

(34) Dai, L.-X.; Wang, X.-Y.; Yang, S.-S.; Zhang, T.; Ren, P.-J.; Ye, J.-Y.; Nan, B.; Wen, X.-D.; Zhou, Z.-Y.; Si, R.; Yan, C.-H.; Zhang, Y.-W. *J. Mater. Chem. A* **2018**, *6* (24), 11270–11280.

(35) Li, M.; Kowal, A.; Sasaki, K.; Marinkovic, N.; Su, D.; Korach, E.; Liu, P.; Adzic, R. R. *Electrochim. Acta* **2010**, *55* (14), 4331–4338.

(36) Xu, C.; Goodman, D. W. *J. Phys. Chem.* **1996**, *100* (1), 245–252.

(37) Geraldes, A. N.; Silva, D. F.; Silva, J. C. M.; Souza, R. F. B.; Spinacé, E. V.; Neto, A. O.; Linardi, M.; Santos, M. C. *J. Braz. Chem. Soc.* **2014**, *25* (5), 831–840.

(38) Yang, Y. Y.; Ren, J.; Li, Q. X.; Zhou, Z. Y.; Sun, S. G.; Cai, W. Bin. *ACS Catal.* **2014**, *4* (3), 798–803.

(39) Gomes, J. F.; Bergamaski, K.; Pinto, M. F. S.; Miranda, P. B. *J. Catal.* **2013**, *302*, 67–82.

(40) Marinković, N. S.; Wang, J. X.; Zajonz, H.; Adžić, R. R. *J. Electroanal. Chem.* **2001**, *500* (1–2), 388–394.

(41) Li, M.; Liu, P.; Adzic, R. R. *J. Phys. Chem. Lett.* **2012**, *3* (23), 3480–3485.

(42) Lopes, P. P.; Strmcnik, D.; Jirkovsky, J. S.; Connell, J. G.; Stamenkovic, V.; Markovic, N. *Catal. Today* **2016**, *262*, 41–47.

(43) Herron, A.; Ferrin, P.; Mavrikakis, M.; Herron, J. A.; Ferrin, P.; Mavrikakis, M. *J. Phys. Chem. C* **2015**, *119* (26), 14692–14701.

(44) Song, L.; Liang, Z.; Ma, Z.; Zhang, Y.; Chen, J.; Adzic, R. R.; Wang, J. X. *J. Electrochem. Soc.* **2018**, *165* (15), J3095–J3100.

(45) Miao, B.; Wu, Z.; Xu, H.; Zhang, M.; Chen, Y.; Wang, L. *Chem. Phys. Lett.* **2017**, *688*, 92–97.

For Table of contents